NMR-crystallographic study of two-dimensionally self-assembled cyclohexane-based low-molecular-mass organic compounds†

Marko Schmidt,[a] Christoph S. Zehe,[a] Renée Siegel,[a] Johannes U. Heigl,[b] Christoph Steinlein,[b] Hans-Werner Schmidt[b] and Jürgen Senker*[a]

Using a combined approach based on scanning electron microscopy, powder X-ray diffraction as well as 1D and 2D multinuclear solid-state NMR spectroscopy, we were able to determine the morphology and the crystal structures for a set of three supramolecular compounds with different hydrogen bonding motifs, namely *N*,*N*'-(cyclohexane-*trans*-1,4-diyl)bis(2,2-dimethylpropanamide) **1**, 1,1'-(cyclohexane-*trans*-1,4-diyl)bis(3-*tert*-butylurea) **2** and N^1,N^4-bis(*tert*-butylcarbamoyl)cyclohexane-*trans*-1,4-dicarboxamide **3**. Based on a complete signal assignment of the 1D solid-state MAS NMR spectra (^{1}H, ^{13}C, ^{15}N) employing 2D HETCOR experiments and a quantitative evaluation of the corresponding resonances, the content of the asymmetric unit was determined to one half of a molecule. Probing the molecular configuration with ^{1}H–^{1}H double-quantum experiments revealed an intramolecular hydrogen bond for compound **3** while **1** and **2** form exclusively intermolecular H-bonds. *Ab initio* structure solutions applying real space methods with an included close-contact penalty were carried out for all compounds. The following Rietveld refinements led to excellent wR_p-values between 2.5% and 4.1%. Compounds **1** and **2** crystallise isostructurally in the monoclinic space group $P2_1/c$ exhibiting a pseudo-biaxial hydrogen bond motif. **3** crystallises in the triclinic space group $P\bar{1}$ with intermolecular head-to-tail hydrogen bonds connecting the molecules to one-dimensional ribbons. Nevertheless, all compounds grow in a sheet-like morphology with lateral dimensions of several hundred micrometres indicating a fast growth in two dimensions along two of the crystal axes. Since all three molecules possess inversion symmetry cancelling the molecular dipole moment the growth mechanism itself has to be dominantly driven by the formation of hydrogen bond networks.

Introduction

Within the last decades the field of supramolecular chemistry has attracted significant attention resulting in the synthesis and design of functional molecules evolving into ordered superstructures *via* self-assembly mechanisms. Driven by non-covalent interactions between the constituent parts,[1] like hydrogen bonding, aromatic π–π stacking, CH–π interactions, electrostatic or hydrophobic interactions, these complex structures offer a wide diversity of functions highlighting the versatility and flexibility within this field of research. The dimensionality of the resulting nanostructures (from one- to three-dimensional), however, plays a fundamental role in order to vary macroscopic properties.

Certain types of supramolecular building blocks form predominantly one-dimensional nanostructures. Here, benzene-1,3,5-tricarboxamides (BTAs) represent an important class and are described in detail by Cantekin *et al.*[2] The choice of appropriate substituents results in a broad range of materials. For example organogels,[3–5] hydrogels,[6,7] discotic liquid crystals,[8] metal complexation[9] and MRI-contrast agents,[10] as well as nucleating agents and clarifiers for semi-crystalline polymers[11–18] have been reported. The hydrogen bond mediated cooperative effect results in the formation of one-dimensional rod-like nanoobjects. The topological arrangement of these columnar nanostructures is dominated by a (pseudo)hexagonal rod packing.[19,20] Since each BTA possesses an intrinsic dipole moment, the build-up of these rods is strongly connected to the formation of a macrodipole with a high intrinsic potential energy.[21] Only the macroscopic compensation of these macrodipoles by neighbouring rods being directed antiparallel and leading to

[a] *Inorganic Chemistry III and Bayreuth Center for Colloids and Interfaces, University of Bayreuth, 95440, Bayreuth, Germany. E-mail: juergen.senker@uni-bayreuth.de; Fax: +49 921-55-2788; Tel: +49 921-55-2532*
[b] *Macromolecular Chemistry I, Bayreuth Institute of Macromolecular Research and Bayreuth Center for Colloids and Interfaces, University of Bayreuth, 95440, Bayreuth, Germany. E-mail: hans-werner.schmidt@uni-bayreuth.de; Fax: +49 921-55-3206*
† Electronic supplementary information (ESI) available. See DOI: 10.1039/c3ce41158c
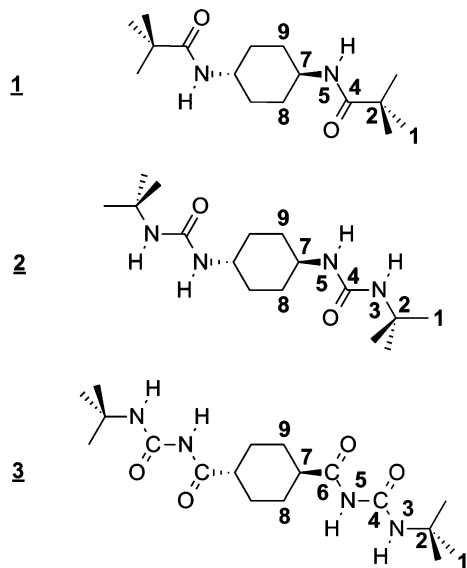
Scheme 1 Chemical structures of *N,N'*-(cyclohexane-*trans*-1,4-diyl)bis(2,2-dimethylpropanamide) **1**, 1,1'-(cyclohexane-*trans*-1,4-diyl)bis(3-*tert*-butylurea) **2** and *N*^{1},*N*^{4}-bis(*tert*-butylcarbamoyl)cyclohexane-*trans*-1,4-dicarboxamide **3** with labelling of the atoms for the NMR signal assignment.

an antiferroelectric arrangement allows for a fast one-dimensional growth.

Recently, two-dimensional nanostructures with a high aspect ratio have gained increasing interest[22] with lateral dimensions ranging from a few hundred nanometres up to the micron scale. Well known inorganic examples are layered silicates[23] and graphene with exceptional properties.[24–29] Lately, a new pathway to two-dimensional nanoobjects has emerged based on supramolecular self-assembly of low-molecular-mass organic molecules (LMOs).[22] Among others, Zentel and co-workers reported a couple of bis-acylurea compounds possessing a C_5 or C_6 alkyl spacer with different functional end groups.[30,31] An in-depth understanding of the formation of these nanosheets is still challenging. It is quite evident that hydrogen bonding is important. However, the role of dipole moments or even macrodipoles as a driving force for the two-dimensional growth is still an open question.

In order to derive a deeper understanding of the structure–property relations of two-dimensional nanosheets, we selected three compounds with different hydrogen bond motifs. The materials (Scheme 1) are based on symmetric substituted *trans*-(1,4)-cyclohexane derivatives with increasing number of donor (NH) and acceptor groups (CO), namely amide **1**, urea **2** and acylurea **3** moieties. We focus on the *ab initio* structure solutions as well as the hydrogen bond networks of these three LMOs. Since the lack of suitable single crystals prevents using single crystal X-ray diffraction experiments, we employ NMR-crystallographic strategies to derive both detailed local and topological features of these compounds. To complement powder diffraction data with solid-state NMR experiments and computational modeling at various steps of the structure

elucidation[32–35] has proven to be an efficient way to validate or disprove structure models.

Experimental section

Materials and instruments

All solvents were purified and dried prior to use according to standard procedures. The starting materials were purchased from ABCR, Acros, Aldrich, and TCI Europe and used as received. Elementary analysis (C, H, N) were carried out using a Vario elementar EL III instrument. Mass spectra were recorded at RT on a FINNIGAN MAT 112S instrument (70 eV) with electronic impact ionisation and direct probe inlet. SEM was performed on a Zeiss 1530 FESEM (3 kV) with a preceding platinum sputtering using a Cressington Sputter Coater 208HR.

Syntheses of 1–3

The general reaction schemes are depicted in Scheme S1 within the ESI.†

N,N'-(Cyclohexane-*trans*-1,4-diyl)bis(2,2-dimethylpropanamide) 1

Compound **1** was synthesised by dropping pivalic acid chloride (7.3 g, 61 mmol) to a mixture of *trans*-1,4-diaminocyclohexane (3 g, 26 mmol), pyridine (10 mL), LiCl (0.05 g) and *N*-methyl-2-pyrrolidone (NMP, 180 mL) at 0 °C under nitrogen atmosphere. The reaction mixture was heated to 80 °C and stirred overnight. The mixture was precipitated in cold water and the white solid was filtered off, dried under vacuum for 2 h (70 °C, 100 mbar) and re-crystallised from methanol. Yield: 4.5 g (16 mmol, 61.5%, based on *trans*-1,4-diaminocyclohexane). Anal. calculated for **1**: C, 68.04; H, 10.71; N, 9.92. Found: C, 67.34; H, 12.23; N, 9.80%. MS (70 eV), *m/z* (%): 282 (M$^+$, 3.3); 197 (10.4); 181 (74.5); 127 (5.7); 102 (100); 85 (9.4); 80 (6.6); 57 (3.8).

1,1'-(Cyclohexane-*trans*-1,4-diyl)bis(3-*tert*-butylurea) 2

Compound **2** was synthesised by dropping *tert*-butyl isocyanate (dissolved in 400 mL THF at room temperature, 5 g, 101 mmol) to a solution of *trans*-1,4-diaminocyclohexane in THF (10 g, 44 mmol) at 0 °C under argon atmosphere. The mixture was stirred overnight at 80 °C, filtered off, dried under vacuum and re-crystallised from methanol. Yield: 12 g (38 mmol, 87.3%, based on *trans*-1,4-diaminocyclohexane). Anal. calculated for **2**: C, 61.5; H, 10.32; N, 17.93. Found: C, 61.17; H, 11.10; N, 17.78%. MS (70 eV), *m/z* (%): 312 (M$^+$, 9.4); 212 (29.2); 197 (18.8); 139 (7.5); 113 (13.2); 96 (18.8); 68 (9.4); 58 (100); 41 (11.3).

N^1,*N*^{4}-Bis(*tert*-butylcarbamoyl)cyclohexane-*trans*-1,4-dicarboxamide 3

Compound **3** was synthesised by dropping a mixture of cyclohexane-*trans*-1,4-dicarbonyl dichloride (3.14 g, 15 mmol) and 3.65 mL pyridine to a solution of 1-*tert*-butyl urea (3.49 g, 30 mmol) in THF at 0 °C under argon atmosphere. The reaction mixture was stirred overnight at 70 °C, filtered off, dried

under vacuum for 2 h at 70 °C and re-crystallised from DMF. Yield: 2.2 g (6 mmol, 40%, based on cyclohexane-*trans*-1,4-dicarbonyl dichloride). Anal. calculated for **3**: C, 58.64; H, 8.75; N, 15.21. Found: C, 58.42; H, 8.81; N, 15.16%. MS (70 eV), *m/z* (%): 353 (M$^+$, 91.5); 313 (4.7); 280 (33.9); 254 (15.1); 240 (7.5); 197 (6.6); 169 (14.1); 126 (29.2); 109 (3.7); 81 (17.9); 59 (100).

Ab initio structure determination with powder X-ray diffraction

PXRD measurements for compounds **1–3** were carried out in Debye–Scherrer geometry on a STOE StadiP diffractometer, which was equipped with Cu Kα_1 radiation ($\lambda = 1.5406$ Å) and a curved germanium monochromator (oriented according to the 111 plane). The samples were filled in capillary tubes with a diameter of 0.5 mm and measured in the 2Θ range of 3–50° with a step size of 0.015°. The powder diffractograms were fully handled using the module REFLEX PLUS from the commercial program package Accelrys MS Modeling (version 5.0).[36] After indexing, Pawley refinement and space group assignment, the structure solution step was performed by means of real-space methods using the parallel tempering algorithm. For every structure solution, the molecule was first geometry optimised using DFT methods (see section Computational methods). As starting models for compounds **1–3** only half a molecule was set into the asymmetric unit as one motion group. Besides the possible rotational and translational degrees of freedom, all sustainable torsion angles in each molecule fragment were set free during the structure solution. Additionally, a preferred orientation model (March–Dollase) was applied during the solution with focus on the shape of the crystallites (R_0) as well as the orientation of the normal of the crystal faces ($a*$, $b*$, $c*$).[37]

For the Rietveld refinement, at first four cycles including a relaxation of atomic parameters, a global isotropic temperature factor and a preferred orientation correction according to the Rietveld–Toraya equation[38,39] were carried out. By taking into account energy considerations using the COMPASS force field,[40] the molecular structure was maintained without limiting rotational and translational degrees of freedom. The resulting number of refined structural parameters (see Table 1) is hence not strictly representative due to the application of the energy constraint during the refinement. This force field assisted refinement is based on a combined figure of merit (R_{comb}) with

$$R_{comb} = (1 - w_{comb})wR_p + w_{comb}R_{Energy} \qquad (1)$$

where w_{comb} represents the energy weighting factor that was set to 0.5. The energetic contribution, R_{Energy}, to the combined figure of merit is defined as follows:

$$R_{Energy} = \tanh\left(0.1\frac{E - E_{min}}{E_{tol}}\right) \qquad (2)$$

where E represents the total energy, E_{min} the energy in the global minimum and E_{tol} the energy window above E_{min} in which possible structure solutions are tolerated. Here, the

Table 1 Relevant crystallographic data for **1–3** from PRXD

	1	2	3
Formula	$C_{16}H_{30}N_2O_2$	$C_{16}H_{32}N_4O_2$	$C_{18}H_{32}N_4O_4$
M/g mol^{-1}	282.42	312.45	368.47
Crystal system	Monoclinic	Monoclinic	Triclinic
Space group	$P2_1/c$	$P2_1/c$	$P\bar{1}$
a/Å	14.183(3)	15.435(7)	6.092(3)
b/Å	6.159(1)	6.762(3)	7.325(4)
c/Å	9.889(2)	8.883(4)	12.473(6)
α/°	90	90	73.828(3)
β/°	98.383(1)	96.343(2)	83.507(3)
γ/°	90	90	87.597(2)
V/Å^3	854.6(8)	921.4(12)	531.1(8)
Z'/Z	0.5/2	0.5/2	0.5/1
ρ/g cm^{-3}	1.097(1)	1.125(2)	1.151(2)
T/K	293	293	293
U	0.20(1)	0.14(1)	0.23(1)
V	−0.021(3)	0.005(3)	−0.012(4)
W	0.0029(2)	0.0013(2)	0.0025(2)
NA	0.42(2)	0.79(4)	0.76(3)
NB	0.001(1)	0.002(2)	0.00(2)
Zero-point shift	−0.031(1)	0.009(1)	−0.021(1)
R_0 ^{a}	0.223	0.654	0.868
$a*$	0.9877(2)	−0.9885(3)	−0.109(5)
$b*$	0.137(1)	0.147(2)	−0.087(9)
$c*$	0.074(1)	0.030(2)	−0.990(1)
No. ref. struct. par.^{b}	81	87	93
R_p	0.0272	0.0217	0.0157
wR_p	0.0411	0.0301	0.0254

^{a} Preferred orientation coefficient of the sample according to the March–Dollase function representing a dimensionless value reflecting the shape of the crystallites; $R_0 < 1$ for platelets, $R_0 > 1$ for needles. ^{b} The number of refined structural parameters includes one isotropic temperature factor and three translational elements of each atom within the asymmetric unit. Since a COMPASS force field with an energy constraint was applied, the refinement of the atomic positions is not handled independently.

default value of 40 kcal mol^{-1} was used prohibiting the breaking of covalent bonds during the refinement and thus reducing the independent number of refined structural parameters markedly.

Afterwards, besides the adjustment of the lattice parameters, the pseudo-Voigt peak profile including FWHM with its profile parameters NA and NB were optimized. The pseudo-Voigt peak shape function as a linear combination of a Gaussian (G) and a Lorentzian (L) includes a Θ-dependent mixing parameter η whose Θ-dependence is thus given by

$$\eta(\Theta) = (NA + NB)2\Theta \qquad (3)$$

where NA and NB are adjustable parameters. Besides, the zero-point shift, sample off-centering, asymmetry correction (Finger–Cox–Jephcoat)[41] and the experimental background using 20 orthogonal polynomials were refined. For both refinement steps, 15 evaluations per cycle per degree of freedom were performed. Relevant crystallographic data are summarized in Table 1. Atomic parameters, the temperature factor and the occupancy of **1–3** are included in the CIF files which are provided in the ESI.†

Solid-state NMR spectroscopy

^{1}H and ^{13}C chemical shifts are referenced to TMS ($\delta_{ref}((^1H_3C)_4Si) = 0$ ppm, $\delta_{ref}((H_3^{13}C)_4Si) = 0$ ppm), ^{15}N

chemical shifts are reported with respect to nitromethane ($\delta_{ref}(H_3C-^{15}NO_2) = 0$ ppm). The spin rate for all MAS experiments was set to $10\,000 \pm 1$ Hz. The 1D ^{1}H-DUMBO and 2D ^{1}H–^{1}H double-quantum-single-quantum (DQ-SQ) correlation experiments were performed on a Bruker Avance III spectrometer at a proton resonance frequency of 400 MHz with a 3.2 mm triple resonance probe. The CP and the HETCOR experiments on ^{13}C and ^{15}N were performed on a Bruker Avance II spectrometer with a proton frequency of 300 MHz using a 4 mm triple resonance probe. For the latter experiments proton broadband decoupling was realised with a SPINAL64 sequence during acquisition. The nutation frequency and pulse length were set to 72 kHz and 5.6 μs (^{15}N)/6.8 μs (^{13}C), respectively.

For the ^{1}H-DUMBO experiments the DUMBO pulse length and the nutation frequency were adjusted to 30.50 μs and 89.3 kHz, respectively. The total window length between the DUMBO pulses during acquisition was set to 5.6 μs with a dead time delay of 1.2 μs before acquiring a point. A CRAMPS scaling factor of $\lambda_{scaling} = 0.5$ was determined on glycine, where all isotropic chemical shifts are well known.[42] Subsequently, the shifts of all ^{1}H DUMBO spectra were corrected accordingly.

In the case of the ^{1}H–^{1}H DQ-SQ correlation experiments, double quantum excitation and reconversion was achieved through the R20$_2^9$ sequence[43] and high resolution in both dimensions through a DUMBO sequence.[44] For the R-elements, 90–270° composite pulses were used with 80 μs excitation/reconversion time (corresponding to 8 R-elements each) and 100 kHz of nutation frequency. The desired coherences were selected through an eight-fold phase cycling. For DUMBO in the indirect dimension the window length was set to 4.6 μs with an increment of three DUMBO cycles, whereas all remaining parameters for DUMBO in both dimensions were the same as in the one-dimensional DUMBO experiments. For both the indirect and direct dimension a scaling factor of $\lambda_{scaling} = 0.5$ was determined as described above.

The 1D CP spectra of ^{13}C and ^{15}N were recorded using a ramp on the proton channel and a contact time of 5 ms with nutation frequencies of 35/45 kHz for ^{15}N/^{13}C. For the ^{1}H–^{15}N/^{13}C HETCOR experiments a DUMBO sequence was applied in the indirect dimension with a pulse length of 28.8 μs, a nutation frequency of 91 kHz, a delay of 2 μs and four/three DUMBO cycles as increment. Magnetization transfer was achieved using the PRESTO-II sequence.[45] It ensures that spin diffusion between the protons during the contact time is suppressed in contrast to conventional magnetisation transfer by CP. For all compounds, the transfer time for PRESTO was set to 178 μs according to 16 R-elements before and after the 90° pulse probing only the closest ^{1}H–^{13}C and ^{1}H–^{15}N distances. Thus, correlation signals only correspond to covalently bonded nuclei. The nutation frequency for ^{1}H and ^{15}N/^{13}C during PRESTO was set to 90 kHz and 39/70 kHz, while the FID was recorded after a spin echo for refocusing the chemical shift interaction. The refocusing period was chosen to one/two rotor periods for ^{15}N/^{13}C, respectively. An eight-fold phase cycling allowed the selection of the desired coherences.

Computational methods

Before the *ab initio* structure solutions of compounds **1–3**, all molecules were geometry optimised by DFT methods using the module DMol3 from the program package Accelrys MS Modeling (version 5.0).[36] Here, the double zeta plus polarisation basis set with the GGA functional PW91 was applied.[46] The self-consistent field (SCF) energy convergence was set to 1.0–6 eV per atom.

Results and discussion

Morphology

Morphological analyses using scanning electron microscopy (SEM) reveal a two-dimensional growth of compounds **1**, **2** and **3**. Large platelets possessing a high aspect ratio were obtained from hot isotropic solutions of butan-2-one with concentrations between 50 and 500 ppm depending on their solubility. Bisamide **1** shows platelets with well-defined edges and a widely homogenous surface (Fig. 1a) whereas bisurea **2** exhibits partly fringed edges but also a homogenous surface (Fig. 1b). At a first glance the bisacylurea **3** shows sharp edges and a homogenous surface as well. However, when magnifying the edge of the platelet, it becomes clear that one platelet consists of several thin sheets (Fig. 1c). In contrast, no fine structure can be determined by using SEM in case of **1** and **2**.

Structural information obtained from solid-state NMR spectroscopy

Compounds **1–3** form only microcrystalline powders preventing structure analysis by single crystal X-ray diffraction. Since this circumstance is not specific for our samples but a common case for organic substances, the development of alternative structure elucidation methods for powder samples is necessary. *Ab initio* structure solutions employing solely PXRD data are often hampered by a severe loss of information. Symmetry equivalent reflexes always coincide and higher order reflexes overlap heavily, reducing the number of independent intensity information.[47] While topological information might still be obtained with reasonable accuracy, local structural details are strongly affected.[34,47] In this context, solid-state NMR spectroscopy provides complementary data and thus evolved into an important element of NMR crystallographic strategies. Meanwhile, solid-state NMR is able to participate in nearly all steps of the structure solution process starting from space group selection, over model building up to the final Rietveld refinement.[19,47–50] Symmetry information including the content of the asymmetric unit might be obtained by deriving Wyckoff spectra[48,51] from high-resolution experiments and by determining rotational symmetry elements[47,52,53] based on orientation correlations of CSA tensors of neighbouring nuclei. Analysing hetero- and homonuclear connectivities, distances, distance sums and even torsion angles measured by 1D and 2D dipolar recoupling experiments support the construction of structure models.[19,20,32–34,49,50] The expressiveness of such measurements is significantly increased by
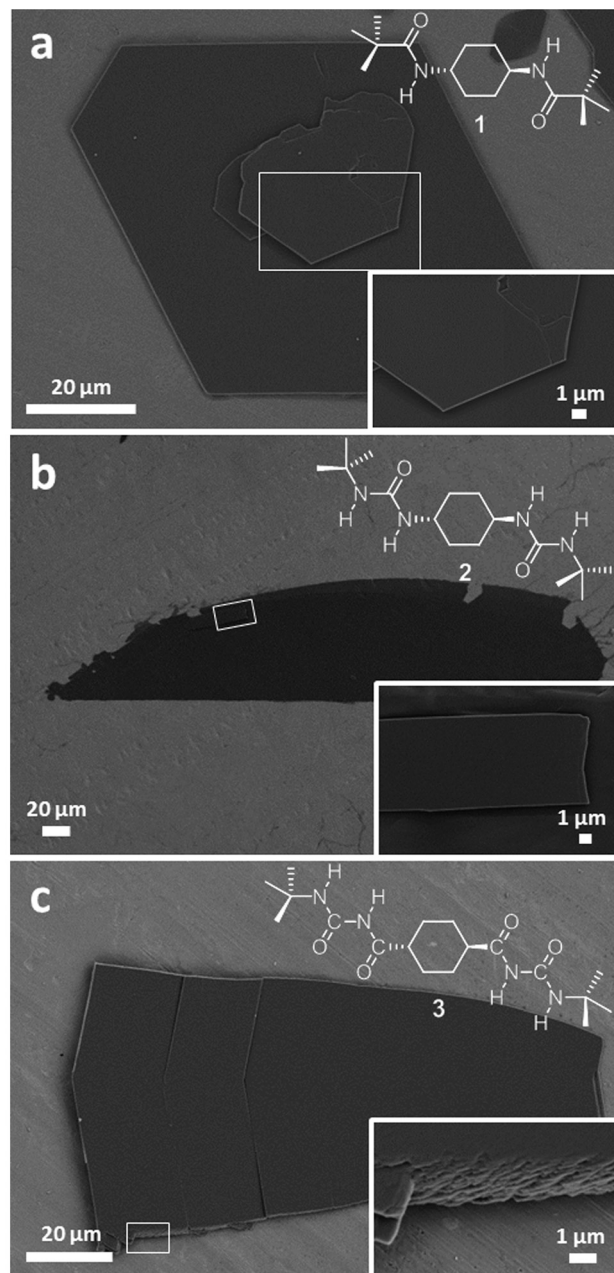
Fig. 1 SEM images of two-dimensional structures of (a) bisamide **1** (500 ppm), (b) bisurea **2** (200 ppm) and (c) bisacylurea **3** (50 ppm) formed in butan-2-one. The regions where the magnified images (insets) have been collected are marked using white boxes.

Fig. 2 1D MAS spectra at v_{MAS} = 10 kHz for compounds **1** (black), **2** (red) and **3** (blue): (a) ^{1}H-DUMBO (B_0 = 9.4 T); the strong signal of the methyl groups is truncated to highlight the weaker resonances, in particular the NH signals; (b) ^{13}C CP-MAS (B_0 = 7.04 T); (c) ^{15}N CP-MAS (B_0 = 7.04 T). For the CRAMPS experiments the chemical shifts are corrected according to glycine ($\lambda_{scaling}$ = 0.5).

combination with quantum chemical calculations.[54,55] For instance, hydrogen bond scenarios can be probed by combining *ab initio* chemical shift calculations and high-resolution NMR measurements.[34,54,56] Even the substructure of light atoms like hydrogen has successfully been determined.[32,50] Since most of these methods require high resolution spectra, hetero- and homonuclear decoupling of strongly coupled spin systems like protons is necessary. Moreover, for a correct interpretation of these spectra, a complete assignment of all signals is essential, which can be obtained through 2D heteronuclear correlation experiments.
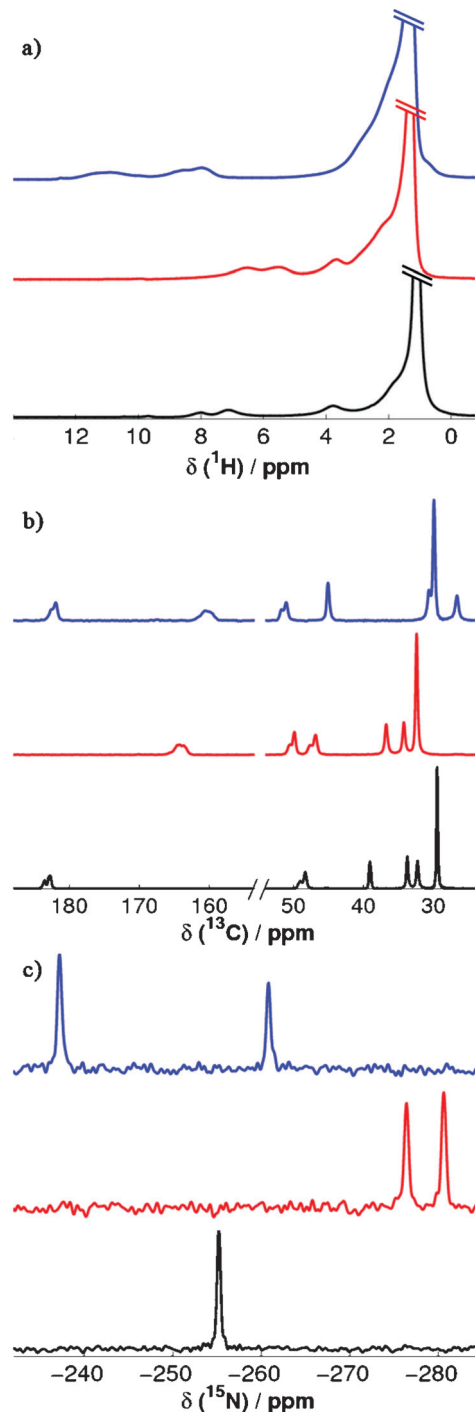
Following this strategy, information about hydrogen bond patterns, configurations and symmetries of the crystal structures of compounds **1–3** are deduced. In particular, we support the *ab initio* structure solutions by PXRD through solid-state NMR experiments on the three NMR-active nuclei
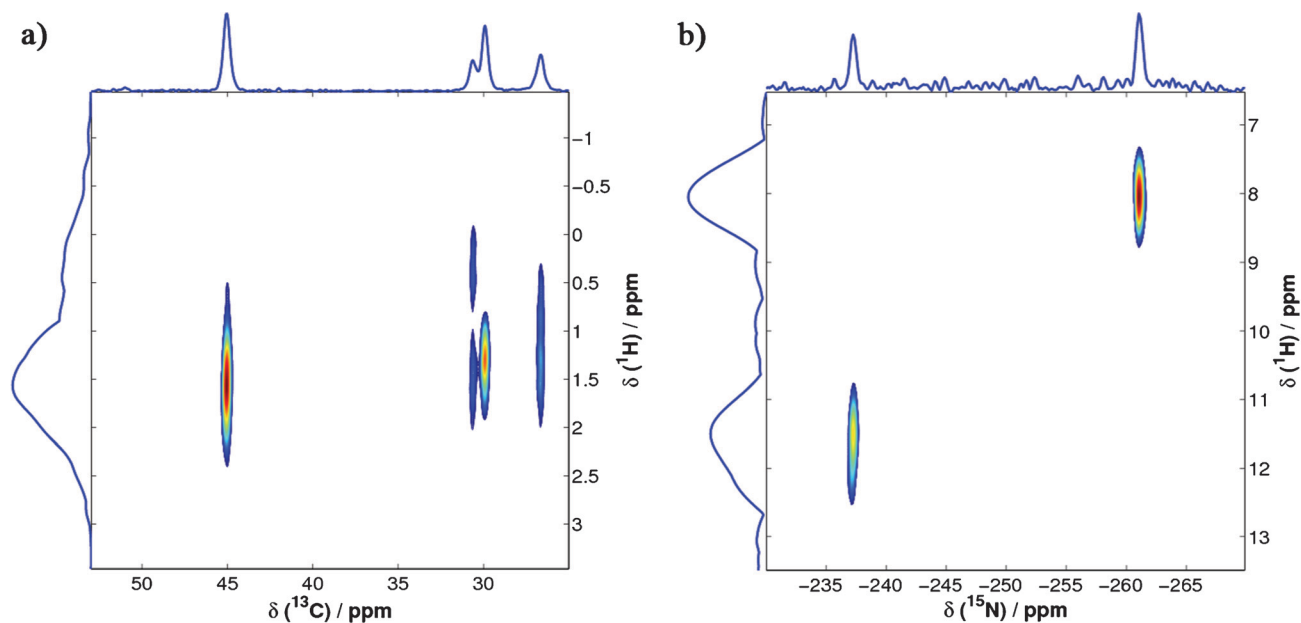
a)   b)

Fig. 3 (a) ^{1}H–^{13}C-HETCOR and (b) ^{1}H–^{15}N-HETCOR spectrum of compound 3, at B_0 = 7.04 T and ν_{MAS} = 10 kHz. The ^{1}H chemical shifts in the f1 domains are corrected according to glycine ($\lambda_{scaling}$ = 0.5). The transfer time was set to 178 μs visualising only directly bonded protons.

^{1}H, ^{13}C and ^{15}N. First, a complete assignment of 1D high-resolution spectra of ^{1}H, ^{13}C, ^{15}N experiments through 2D ^{1}H–^{13}C and ^{1}H–^{15}N HETCOR spectra is conducted. Fig. 2 depicts high-resolution 1D spectra of ^{1}H, ^{13}C and ^{15}N for all three compounds. The assignment will be done exemplarily for compound 3, since the procedure for the remaining samples is almost identical. The 2D ^{1}H–^{13}C-HETCOR and ^{1}H–^{15}N-HETCOR experiments for that purpose are pictured in Fig. 3a and 3b.

The ^{1}H-DUMBO spectrum of 3 shows a sharp, intense peak at δ = 1.3 ppm (Fig. 2a). This signal couples in the ^{1}H–^{13}C-HETCOR to a carbon signal at δ = 29.9 ppm (Fig. 3a). Both the ^{13}C and ^{1}H shifts are indicative for CH_3 groups. Moreover, the sharpness and high intensity of both peaks are characteristic for CH_3 for the following reasons: first, the well-known rotation of the groups around the C–CH_3 bond truncates dipolar coupling to other spins, which raises the transversal relaxation time and thus reduces the width of the peaks for both spins. Second, the high abundance of CH_3 protons increases their signals in DUMBO as well as in ^{13}C CP. The carbon signals at δ = 30.6 ppm and – remarkably shielded – at δ = 26.6 ppm correspond to the two different sets of CH_2 groups within the cyclohexane ring, one carbon signal with couplings to the resolved proton shifts at δ = 0.4 and 1.6 ppm, the other one with two overlapping proton signals at *ca.* δ = 0.8 and 1.3 ppm. The CH unit of the ring is assigned to the more deshielded peak at δ = 1.6 ppm for ^{1}H, coupling to the carbon signal at δ = 45.0 ppm, since both carbon and proton shifts are typical for CH groups. The remaining signals in the ^{13}C CP (Fig. 2b, δ = 51.2 ppm, 155.3 ppm and 177.2 ppm) do not give rise to cross correlation peaks in the ^{1}H–^{13}C-HETCOR and are thus not covalently bonded to protons. The peak at δ = 51.2 ppm in the ^{13}C CP spectrum is unequivocally

assigned to the quaternary carbon atom of the *tert*-butyl group while the two remaining signals at δ = 155.3 ppm and 177.2 ppm belong to the C=O groups. A comparison of their line shapes observed at different magnetic fields of 7.1 T and 9.4 T, respectively, reveals an inverse dependence of the splitting on the field strength. This line shape is, therefore, caused by second order quadrupolar interaction between the neighbouring ^{14}N nucleus and the ^{13}C spins.[57] This was also reproduced by simulations of 1D spectra for a ^{13}C–^{14}N spin pair with the program WSOLIDS1 (see Fig. S2b in the ESI†).[20,58]

To assign the remaining peaks in the ^{1}H-DUMBO at δ = 8.0 ppm, 8.6 ppm and 11.2 ppm, ^{1}H–^{15}N HETCOR experiments were performed (Fig. 3b). The ^{15}N CP spectrum of 3 (Fig. 2c) reveals two different peaks at δ = −237.2 ppm and −261.0 ppm. Here, the ^{15}N site at δ = −261.0 ppm shows correlations with a single proton signal at δ = 8.4 ppm. Since already the carbon atoms directly bound to a nitrogen atom were influenced through second order quadrupolar interaction, a single-pulse experiment under MAS at a higher magnetic field strength and a line shape simulation using WSOLIDS1 were conducted (Fig. S1 and Table S1 in the ESI†).[58] It becomes clear that the two peaks at δ = 8.0 and 8.6 ppm correspond to a single proton with an isotropic shift of δ = 8.4 ppm. This effect is well-known for NH groups.[57] The remaining ^{15}N signal at δ = −237.2 ppm shows only one correlation in the ^{1}H–^{15}N HETCOR to the proton signal at δ = 11.2 ppm and thus corresponds to the second NH group.

In order to assign the two carbonyl and the two NH signals to the corresponding chemical units, the experimental resonances were compared to chemical shifts in solution-state NMR, being calculated based on an increment system according to ref. 58 (see Table S2 in the ESI†).[59] Here, the carbon groups C_4 and C_6 of the acylurea group which are

Table 2 Chemical shifts in ppm for all ^1H, ^{13}C and ^{15}N of compounds **1–3** (for labelling see Scheme 1). The asterisks indicate average shifts for cases where the corresponding signals show a splitting due to second order quadrupolar interaction with ^{14}N. All spectra used for assignment of **1** and **2** are contained in the ESI† (Fig. S3 and S4)

Atom	1	2	3	Unit
C_1	29.5	32.4	29.9	CH_3
C_2	39.0	50.0*	51.2*	C_q
C_4	178.2*	159.2*	155.3*	C=O
C_6	—	—	177.2*	C=O
C_7	48.7*	47.2*	45.0	CH
C_8	32.3	34.2	26.6	CH_2
C_9	33.7	36.7	30.6	CH_2
N_3	—	−280.6	−261.0	NH
N_5	−255.2	−276.4	−237.2	NH
H_1	1.1	1.3	1.3	CH_3
H_3	—	6.0*	8.4*	NH
H_5	7.4*	6.1*	11.2	NH
H_7	3.5	3.3	1.6	CH
H_8	1.4	0.5/1.0	0.8/1.3	CH_2
H_9	1.0	1.0/1.5	0.4/1.6	CH_2

connected to the *tert*-butyl unit and the cyclohexane ring, respectively, show a shift of $\delta = 155.7$ ppm and $\delta = 179.4$ ppm, which is close to the observed shifts of $\delta = 155.3$ ppm and 177.2 ppm in the solids. In the case of ^{15}N, for the two nitrogen atoms N_3 and N_5 shifts of $\delta = −277.2$ ppm and −246.0 ppm are predicted, whereas the observed shifts are $\delta = −261.0$ ppm and −237.2 ppm. Considering that the solid-state shifts of ^{15}N in NH groups are usually influenced more strongly by *e.g.* hydrogen bonds than in the case of ^{13}C, the predicted values show a sufficient agreement with the observed ones.

Thus, all signals in the 1D ^1H, ^{13}C and ^{15}N spectra have unequivocally been assigned to the molecular units of compound **3**. This procedure was also applied to compounds **1**

and **2**. The corresponding values for the chemical shifts are summarized in Table 2.

The 1D CP spectra of ^{15}N show only one NH peak for compound **1** and two peaks for **2** and **3**. The molecular structures, however, exhibit two nitrogen atoms in the case of **1** and four in the case of **2** and **3**. The same comparison applies for the 1D CP spectra of ^{13}C and the ^1H-DUMBO, where the structures always show twice the number of groups than the number of observed resonances. Thus, the asymmetric unit contains just half a molecule and, therefore, both molecular and space group symmetry include a two-fold axis or an inversion centre. The number of possible space groups for structure solutions is thus reduced which will be discussed at a later point.

In order to gain information about spatial proximities of NH protons and thus also possible hydrogen bond patterns of the molecules, we used ^1H–^1H DQ-SQ correlation experiments. The NH regions of these spectra are exemplarily depicted in Fig. 4 for compound **2** and **3** (for compound **1** see Fig. S5 in the ESI†).

For compound **2**, both peaks around $\delta = 5.4$ ppm and 6.4 ppm correspond to two overlapping NH signals of the urea unit with isotropic shifts of $\delta = 6.0$ ppm and 6.1 ppm (extracted from ^1H–^{15}N HETCOR, see Fig. S4 in the ESI†), both split by the neighbouring ^{14}N (see Table 2). Besides correlations of the NH protons to the aliphatic region (see Fig. S6 in the ESI†), correlations of the NH signals among themselves between $\delta = 10.8$ ppm and 12.8 ppm in the double-quantum dimension are observed. Since the line shapes are affected by the ^{14}N nuclei, we cannot distinguish between cross correlations and autocorrelations. However, both cases indicate spatial proximity of NH protons to other
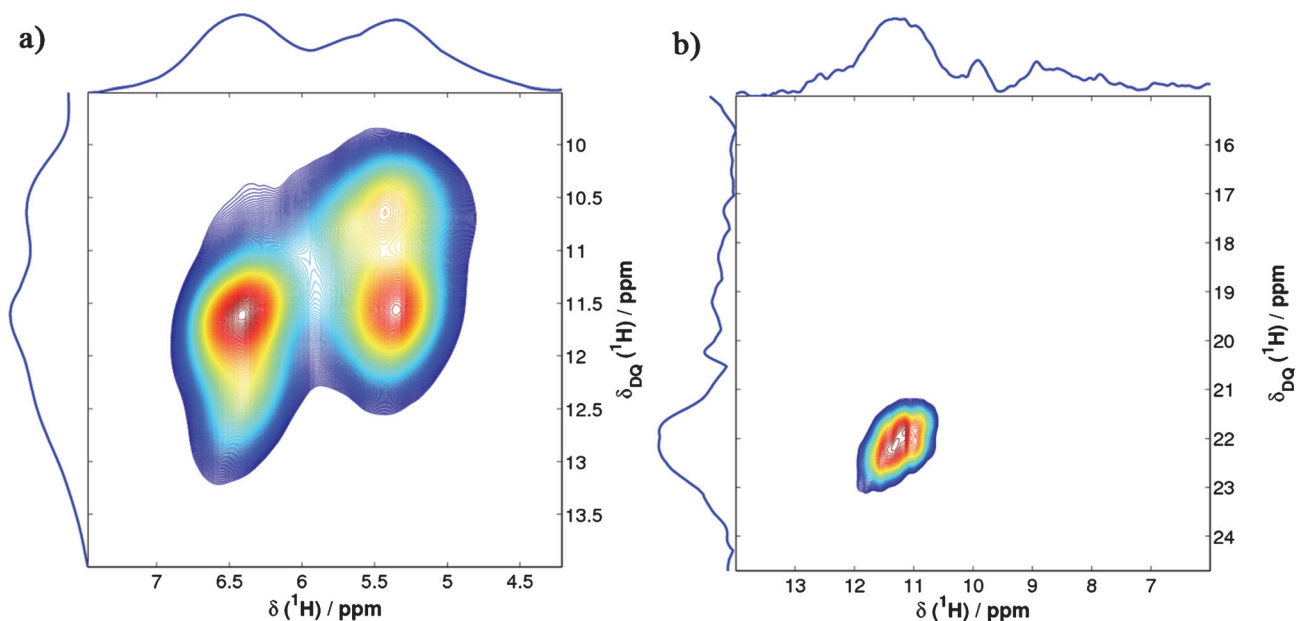

Fig. 4 ^1H–^1H DQ-SQ correlation spectra of (a) compound **2** and (b) compound **3** at $B_0 = 9.4$ T and $\nu_{MAS} = 10$ kHz. The excitation and reconversion time was set to 80 μs in both cases for which only the shortest distance correlations are observed. Both chemical shifts of f1 and f2 are corrected according to glycine ($\lambda_{scaling} = 0.5$). Here, the region around the NH protons is shown (the whole spectra are depicted in Fig. S6 and S7 in the ESI†).
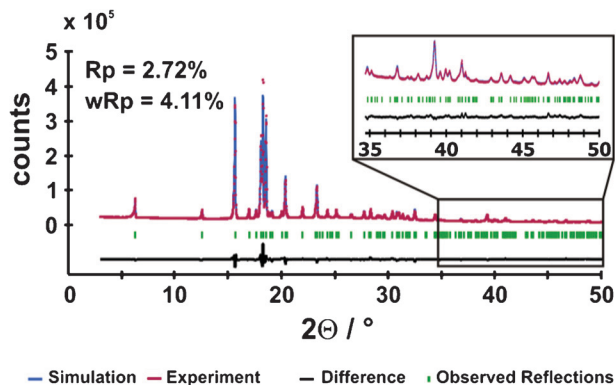
Fig. 5 Rietveld profile plot of the powder X-ray diffraction pattern of **1** for the solution in space group $P2_1/c$ collected at room temperature in the 2Θ range 3–50°. The section of the 2Θ range of 35–50° shows that even at high 2Θ values the simulation fits excellently to the experimental powder pattern.

NH protons. Since the NH units in urea groups usually favour a *trans–trans* configuration each with the connected carbonyl group (*e.g.* as depicted in Scheme 1 for compound **2**) due to energetic reasons, typical H–H distances for this configuration score around 2 Å.[60] Strong DQ coherences as detected in Fig. 4a for **2** are thus characteristic for such short distance.

In contrast, for compound **3** only one weak autocorrelation signal is observed for the NH proton H_5 (δ(SQ/DQ) = 11.4 ppm/22.8 ppm). First, this clearly indicates a spatial proximity between H_5 protons of the inner NH groups. This is only possible when neighbouring molecules are arranged in a hydrogen bond pattern. Second, for the NH signal of proton H_3 at δ = 8.4 ppm no self-correlation signal is observed (δ(DQ, theo) = 16.8 ppm) and thus the intermolecular distances of H_3 protons have to be much longer compared to the ones of H_5. Additionally, no correlation between H_3 and H_5 was detected either (δ(DQ,theo) = 19.9 ppm). This implies a long intermolecular distance between those NH protons of the same acylurea unit (d > 2 Å) and thus allows determining the molecular configuration. In compound **3** just an additional C=O group is inserted compared to **2** (acylurea compared to urea unit). For an all-*trans* configuration of the acylurea group again a distance around 2 Å between H_3 and H_5 and, therefore, an intense DQ correlation signal similar to Fig. 4a is expected. However, a *trans–cis–trans* configuration leads to a distance of more than 3.5 Å rendering the H_3–H_5 DQ correlation unobservable under the chosen experimental conditions. The resulting spatial proximity between the oxygen atom of the inner C=O group and the NH proton H_3 favours the formation of an intramolecular hydrogen bond which might stabilise this configuration. The encapsulation of H_3 in this intramolecular hydrogen bond might also explain the absence of any autocorrelation signal. These results indicate a pair-like arrangement of the molecules within the crystal structure.

Structural information obtained by powder X-ray diffraction

The crystal structures for **1**–**3** were all obtained by *ab initio* structure solutions based on powder X-ray diffraction applying real-space methods using the combination of a close-contact penalty and wR_p, respectively, as cost functions. All molecules were DFT geometry optimised before performing the structure solutions revealing in all cases a chair conformation of the cyclohexane ring as well as C_i symmetry which is energetically favoured over the also previously discussed C_2 symmetry. The inversion centre is thereby positioned in the centre of gravity of the cyclohexane ring. In accordance to the ^{1}H–^{1}H DQ-SQ experiments the *trans–cis–trans* configuration of the acylurea unit in compound **3** revealed the lowest energy during DFT optimisation.

$C_{16}H_{30}N_2O_2$ **1** and $C_{16}H_{32}N_4O_2$ **2**. The indexing of the powder patterns lead unequivocally to a monoclinic metric in both cases and could subsequently be refined in $P2$ using the Pawley algorithm. Assuming that all non-hydrogen atoms within these compounds possess a volume of roughly 18 Å^3, the molecular volumes can be estimated to 360 Å^3 and 396 Å^3, respectively. This size restriction just allows for two molecules within the unit cell at maximum. The reflection conditions do not provide reasonable results for any of the five C-centred space groups but, nevertheless, all remaining 8 primitive ones might be possible. However, based on the symmetry considerations obtained by 1D ^{15}N and ^{13}C solid-state NMR (compare Fig. 3b and 3c) whereupon only half a molecule is located in the asymmetric unit, all possible space groups with the multiplicity of 2 on general positions ($P2$, $P2_1$, Pm and Pc) – then leading to only one molecule in the unit cell – could be excluded. Therefore, only four space groups ($P2/m$, $P2_1/m$, $P2/c$ and $P2_1/c$) remained and, taking into account the reflection conditions, $P2_1/c$ fitted the experimental powder pattern best.

The structure solutions with subsequent Rietveld refinement reveal that **1** and **2** are isostructural and crystallise in the monoclinic space group $P2_1/c$ (for crystallographic information: see Table 1 in the experimental details section). Representative for both compounds, the Rietveld profile plot for **1** is depicted in Fig. 5 (the Rietveld profile plot for **2** is visualised in Fig. S8 in the ESI†). The *a*-axis of **2** is roughly 1.2 Å longer than for **1** while the *c*-axis is shortened by *ca.* 1 Å. The monoclinic angle is slightly reduced by 2° resulting in an increased cell volume of about 65 Å^3 which perfectly agrees with the volume requirement of two additional NH groups.

Fig. 6 shows the molecular crystal structure as well as extended packing plots of *N,N'*-(cyclohexane-*trans*-1,4-diyl)bis(2,2-dimethylpropanamide) **1**. Here, the cyclohexane ring exists in the low-energy chair conformation while the (1,4)-amide linkage exhibits *trans*-configuration on the tertiary carbon atom in the ring as synthesised. The internal $H_4N_4C_4O_4$ torsion angle within the molecule picturing the amide bond is 179.5° which is close to 180° as expected for an amide function (see Fig. 6a) leading to almost coplanarity caused by the inversion symmetry of the molecule itself.

The bisamide compound is characterised by an extended 2D hydrogen bond network. Due to the internal C_i symmetry, only one NH···O length of 2.11 Å is observed. The corresponding N···O distance amounts to 3.1 Å while the NH···O angle of almost 167° is only slightly below the ideal value of 180° demonstrating medium-strong hydrogen bonds. The *trans*-configuration
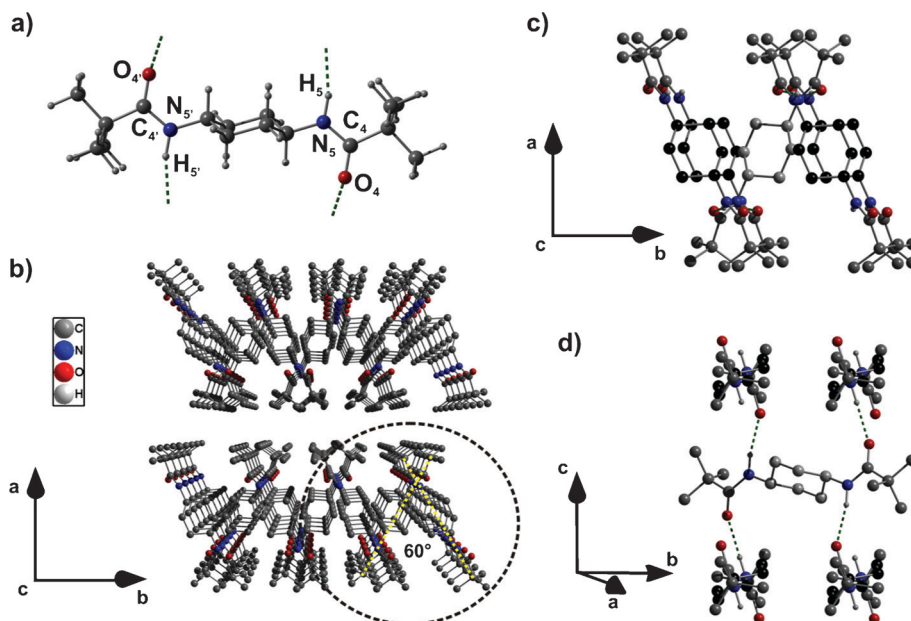
Fig. 6 Molecular structure and extended crystal packing plots of compound **1** with hydrogen bonds highlighted in green dashed lines. (a) Molecular structure of **1** represented with all four hydrogen bond interactions with labelling of the amide function as performed in Scheme 1. (b) Section of the crystal structure viewing along the *c*-axis. The dashed yellow lines represent the opening angle of the molecules main axes projected into the *ab*-plane of the crystal. (c) Cutout of the structure presented in panel b (black dashed circle) showing that one molecule (grey cyclohexane carbon atoms) is enclosed by four molecules (black cyclohexane carbon atoms), two below and two above. This cutout is rotated by 5° along the *b*-axis. (d) Packing plot showing that every molecule builds hydrogen bonds to four neighbouring molecules in one direction. This packing plot is obtained by −90° rotation along the *a*-axis followed by a −35° rotation along the *b*-axis as presented in panel c. All hydrogen atoms except the nitrogen-bonded ones have been omitted in (b)–(d) for clarity.

of the amide functions hence guarantees the formation of two H-bond strands in one direction which is schematically depicted in Fig. 6a.

The propagating direction of the H-bond strands is thereby aligned parallel to the *c*-axis of the crystal leading to a fast growth along this crystal axis. A closer look on the packing motif reveals two additional important features. First, both molecules within the unit cell are twisted towards each other. When assuming a straight line along the main axis of each molecule propagating through the quaternary carbon atoms of the *t*-butyl group followed by a projection into the *ab*-plane of the crystal, an opening angle of 60° is obtained (see Fig. 6b, yellow dashed lines). Second, each amide function within one molecule (NH/CO as donor/acceptor) is connected to one independent counterpart within another molecule. So, every molecule is attached to four neighbouring molecules (see Fig. 6c and 6d) where one donor group interacts with one acceptor group (and *vice versa*). Due to the twist of the molecules, however, a second 'indirect' propagation direction along the *b*-axis that also possesses the tendency of growing fast is observed. Since along the crystals' *a*-axis only van der Waals interactions seem to play the major role – the shortest proton–proton distance being obtained along this crystal axis amounts to 2.44 Å – the corresponding rate of growth is much smaller compared to the growth along the *b*- and *c*-axis, respectively.

Analogous results are obtained for the bisurea compound **2** with an identical molecular geometry as observed for **1** (see Fig. 7a). Nevertheless, the urea group is not perfectly planar with corresponding torsion angles ($H_3N_3C_4O_4$ and $H_5N_5C_4O_4$)

of almost 167°. So, the oxygen atom of the carbonyl group is shifted slightly out of the planar $H_3N_3C_4N_5H_5$-plane in order to form a hydrogen bond network properly. Since one urea group possesses two NH-donor groups, two different H-bond lengths might be observed. Nevertheless, the two bonds are almost equal with bond lengths of 2.19 Å and 2.23 Å, which is consistent with the results extracted from the ^1H and ^{15}N chemical shifts (compare Fig. 2a and 2b), while the corresponding N⋯O distances result in 3.13 Å and 3.17 Å. All these distances are slightly longer than found for the bisamide **1**. This tendency is also true for the related NH⋯O angles which are 154.2° and 153.5°. Therefore, the hydrogen bonds for the bisurea are supposed to be weaker than the ones obtained for the bisamide. However, the H-bond pattern obtained for **2** is more complex than for **1** due to the additional NH group. Compared to **1**, the urea group undertakes the same role as the amide function. Therefore, one acceptor carbonyl group is connected to two NH-donor groups and *vice versa* so that one molecule is H-bond connected to four neighbouring molecules, too (see Fig. 7c and 7d).

This is, for example, in contrast to other bisurea compounds where each molecule is hydrogen-bonded to only two other molecules placed below and above it to self-assemble into 1D fibrillar aggregates.[60,61] Nevertheless, the nature of the urea group itself enables the molecules to form again two H-bond strands as already observed for compound **1**. The propagation direction can also be described as parallel to the *c*-axis of the crystal, so a comparable fast growth in this direction is obtained. Moreover, since also an opening angle
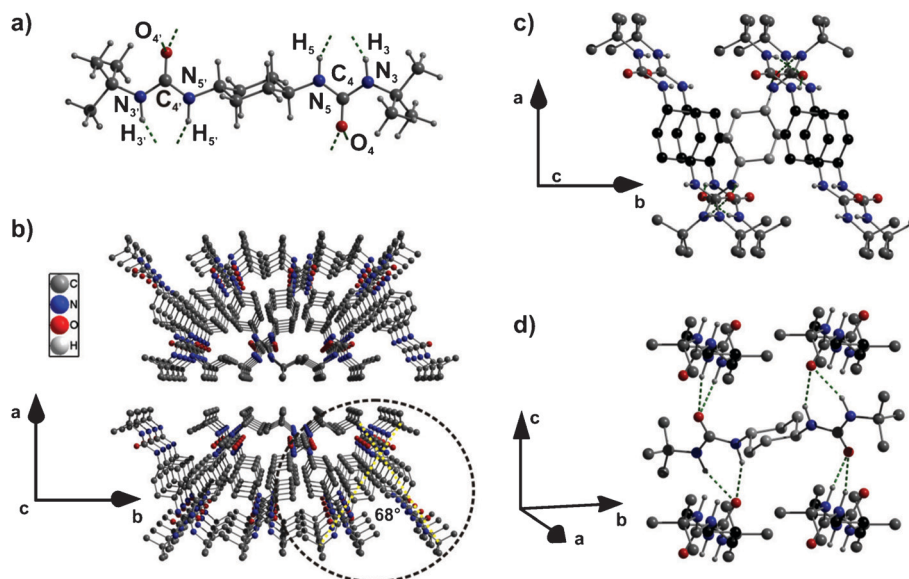
Fig. 7 Molecular structure and extended crystal packing plots of compound **2** with hydrogen bonds highlighted in green dashed lines. (a) Molecular structure of **2** represented with all eight hydrogen bond interactions with labelling of the amide function as performed in Scheme 1. (b) Section of the crystal structure viewing along the *c*-axis. The dashed yellow lines represent the opening angle of the molecules main axes projected into the *ab*-plane of the crystal. (c) Cutout of the structure presented in panel b (black dashed circle) showing that one molecule (grey cyclohexane carbon atoms) is enclosed by four molecules (black cyclohexane carbon atoms), two below and two above. This cutout is rotated by 5° along the *b*-axis. (d) Packing plot showing that every molecule builds hydrogen bonds to four neighbouring molecules in one direction. This packing plot is obtained by −90° rotation along the *a*-axis followed by a −25° rotation along the *b*-axis as presented in panel c. All hydrogen atoms except the nitrogen-bonded ones have been omitted in (b)–(d) for clarity.

between the two twisted molecules within the unit cell of 68° is observed (see Fig. 7b, yellow dashed lines), a second fast growth direction along the *b*-axis is ensured. The discrepancy of 8° is based on the increased length of the bisurea molecule with its accompanying H-bond capabilities that need a broadening of this angle to achieve a sufficient donor–acceptor interaction. Due to the van der Waals forces as the dominating interaction along the crystals' *a*-axis – as already observed for **1** – a fast growth in this direction is inhibited. Here, the shortest intermolecular proton–proton distance with 2.46 Å is thereby identical as obtained for the bisamide.

$C_{18}H_{32}N_4O_4$ **3**. The indexing of the powder pattern of compound **3** revealed a triclinic metric that was successfully refined in *P*1 using the Pawley algorithm. Based on the symmetry information obtained by the 1D ^{15}N and ^{13}C spectra (Fig. 2b and 2c), respectively, where the content of the asymmetric unit was limited to half a molecule, $P\bar{1}$ was considered to be the correct space group. Therefore, **3** crystallises in $P\bar{1}$ with crystallographic data summarised in Table 1. The Rietveld profile plot is depicted in Fig. S9 in the ESI.†

The unit cell consists of one C_i-symmetric molecule based on only half a crystallographic independent molecule in the asymmetric unit. The molecule itself possesses similar structural behaviour as already obtained for compounds **1** and **2** (chair conformation of the cyclohexane ring, see Fig. 8a). The acylurea unit itself is perfectly planar with amide torsion angles of 178.8° ($H_3N_3C_4O_4$ and $H_5N_5C_6O_6$, both *trans*-configured) and 0.8° ($H_5N_5C_4O_4$, *cis*-configured) respectively, leading to a perfect coplanarity (see Fig. 8a). Furthermore, the directly bonded non-urea carboxylic group is

twisted towards the cyclohexane ring with a torsion angle ($H_7C_7C_6O_6$) of almost 133°. This alignment far beyond the ideal 180° might explain the significant shielding of the CH₂ group with a chemical shift of $\delta = 26.6$ ppm obtained in the ^{13}C CP spectrum (see Fig. 2b) and, moreover, can guarantee the formation of an H-bond network which will be discussed later. As already confirmed by $^{1}H–^{1}H$ DQ-SQ solid-state NMR (see Fig. 4, right side) and strongly supported by the DFT geometry optimisation, the acylurea unit possesses a *trans–cis–trans* configuration (Fig. 8a). Here, an intrinsic (1,6)-hydrogen bond with a length of 1.96 Å forming a stable six-membered ring is built. The corresponding N⋯O distance as well as the NH⋯O angle are 2.69 Å and 126°.

In 2007, Davis *et al.* reported the structure of a similar bisacylurea compound obtained by single crystal X-ray diffraction where an aliphatic pentyl group was chosen as a linker between the acylurea groups (BUC5BU).[31] Here, the molecule possesses an intrinsic C_2 symmetry with the same configuration of the acylurea group as observed for our molecule. The two-fold axis thereby propagates directly through the middle carbon atom of the C_5 linking unit.

Beyond that, the *cis* HNCO units forming the intramolecular hydrogen bond point in the same direction as in contrast to the C_i symmetric compound **3** (see Fig. 8b). However, the intramolecular H-bond distance of 2.09 Å and the corresponding N⋯O distance of 2.74 Å is longer than observed for the cyclohexane derivative while, surprisingly, the NH⋯O angle (128.6°) is larger. When comparing the planarity, it becomes obvious that the acylurea group of the BUC5BU compound is slightly out of plane with torsion angles of 169.9° ($H_5N_5C_6O_6$, *trans*),
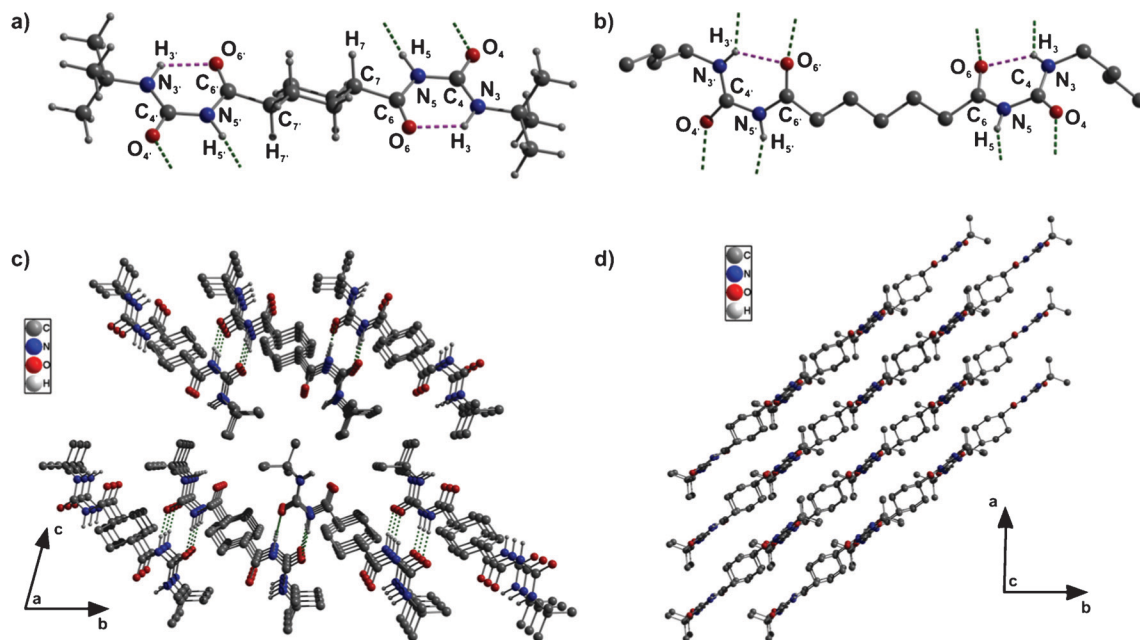
Fig. 8 Molecular structures of compound **3** (a) and BUC5BU[31] (b) represented with intra- and intermolecular hydrogen bonds (dashed pink and green lines, respectively) with labelling of the acylurea units as performed in Scheme 1. (c) Section of the crystal structure of **3** viewed along the *a*-axis. The dashed green lines represent the intermolecular hydrogen bonds to two neighbouring molecules parallel to the crystals' *c*-axis. (d) Section of the crystal structure of **3** viewed along the *c*-axis. This packing plot is obtained by 100° rotation along the *a*-axis, followed by a small rotation (−10°) along the *b*-axis. All hydrogen atoms except the nitrogen-bonded ones have been omitted in (c) and (d) for clarity.

3.9° ($H_5N_5C_4O_4$, *cis*) and 180° ($H_3N_3C_4O_4$, *trans*), respectively, analogous to the angles obtained for **3**. But, moreover, the acylurea moieties of the molecule do show a non-coplanarity with a mutual interplanar angle of 43.3°.

The crystal structure of **3** is schematically pictured in Fig. 8c and 8d. According to the H-bond pattern, it is worth mentioning that only the *cis*-configured amide functions participate in two intermolecular hydrogen bonds each forming in principle one intermolecular six-membered ring (similar to the one already observed in case of the intramolecular H-bond). Interestingly, the corresponding counterpart within a neighbouring molecule also belongs to the *cis*-configured amide function (see Scheme 2a). The number of neighbouring molecules for each molecule therefore is two, which is in contrast to the ones obtained for the compounds **1** and **2**. This alignment in pairs could already be validated by ^1H–^1H DQ-SQ solid-state NMR experiments (see Fig. 4). While no cross correlation signal between the two different NH-protons (H_3 and H_5) was observed since the proton–proton distance of ~3.6 Å is too long, an auto correlation signal for the NH-protons H_5 was found ($d(H_5-H_5$ = 2.5 Å). In case of the BUC5BU compound from ref. 31, however, a similar ^1H–^1H DQ-SQ spectrum as obtained for compound **2** could be expected (compare Fig. 4a), since an intermolecular H_3–H_5 distance of ~3 Å might still be detectable within the applied excitation time.

However, an extensive 2D hydrogen bond pattern – as observed for **1** and **2** – is impossible to realise due to this intermolecular *cis*-arrangement of the amide functions (compare Scheme 2a). Nevertheless, the obtained H-bond of 1.75 Å is very short with an N···O distance of 2.75 Å and, therefore, has to be categorised as strong which is in very good

agreement with the chemical shift of roughly δ = 11.4 ppm for this NH-proton obtained in the 1D ^1H solid-state NMR spectrum (see Table 2). This fact is, furthermore, corroborated by the NH···O angle of 174° which is very close to the ideal 180°. The direction of the intermolecular hydrogen bonds is therefore parallel to the *c*-axis of the crystal. Since only three molecules are involved in this pattern, the self-assembly can – per definition – only be described as classical monoaxial. Though, the self-assembly direction is established by stepwise adding of new molecules along the crystals' *b*-axis *via* hydrogen bonds and, therefore, the fast growth is also observed along this axis. Nevertheless, since the molecules themselves are twisted by almost 45° compared to both the H-bond direction (*c*-axis) as well as the growth direction (*b*-axis), a two-dimensional morphology as observed in SEM can still be obtained (see Fig. 8d).
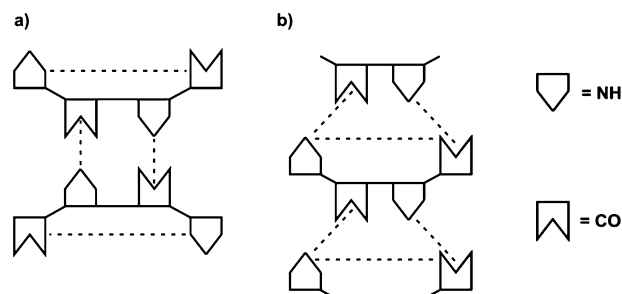
Scheme 2 Donor–acceptor interactions observed for (a) compound **3** forming one intra- and two intermolecular hydrogen bonds per half molecule and (b) BUC5BU forming one intra- and four intermolecular hydrogen bonds per half molecule. The black dashed lines represent the hydrogen bonds between the NH- and CO-groups.

In comparison, the BUC5BU structure presented in ref. 31 shows a different hydrogen bond pattern. It is evident that the *cis*-configured amide function ($O_4C_4N_5H_5$) builds intermolecular hydrogen bonds, but they are not connected to other *cis*-configured amide functions but rather with the appropriate donor/acceptor counterpart that also forms the intramolecular H-bond (see Scheme 2b). So, in principle every molecule is involved in four six-membered rings, two intramolecular and four intermolecular ones. Here, the correspondent hydrogen bond lengths result in 2.11 Å and 2.16 Å, respectively, while the N⋯O distances of 2.88 Å and 2.99 Å are much longer than observed for the cyclohexane derivative 3. Interestingly, the particular NH⋯O angles are 135° and 159°, respectively, suggesting that the intermolecular H-bonds for our bisacylurea compound are much stronger than observed for BUC5BU. Nevertheless, the compound investigated by Davis *et al.* possesses a classic biaxial hydrogen bond system where each BUC5BU molecule is hydrogen-bonded to four adjacent molecules as already described for 1 and 2. This, however, might be caused due to the intrinsic molecular C_2 symmetry while a centrosymmetric molecular symmetry (compound 3) leads only to a classical monoaxial hydrogen bond system.

Conclusion

In summary, three cyclohexane-based compounds with different hydrogen bond motifs were characterised by scanning electron microscopy, solid-state NMR, PXRD and computational methods based on DFT. SEM measurements revealed sheet-like morphologies for all three compounds with lateral dimensions of several hundred micrometres with substantial aspect ratios. The crystal structures of those compounds were elucidated by means of NMR-crystallographic strategies. Based on an unequivocal signal assignment of the 1D spectra by performing ^{1}H–^{13}C- and ^{1}H–^{15}N HETCOR experiments also considering the ^{1}H/^{14}N- and ^{13}C/^{14}N second-order quadrupolar interaction we were able to restrict the space group symmetry and to determine the content of the asymmetric unit. The evaluation of ^{1}H–^{1}H DQ-SQ spectra revealed spatial proton–proton connectivities of the NH groups for all compounds. Additionally for compound 3, they allowed probing both the molecular configuration such as the existence of the intramolecular hydrogen bond and the local environment like the H-bond pattern leading to a pair-like molecular arrangement. This information was crucial to make the *ab initio* structure solutions by real-space methods more efficient and remove ambiguities.

Compounds 1 and 2 crystallise in $P2_1/c$ and their crystal structures exhibit an interesting "pseudo-biaxial" hydrogen bond system where each molecule is directly connected to four neighbouring molecules *via* moderate H-bonds. Caused by the crossed alignment of the molecules within the unit cell (see Fig. 6d and 7d), the H-bond mediated strands are growing fast in two directions even though both H-bond strands are parallel, while the growth in the third dimension is retarded resulting in two-dimensional nanosheets. Although such a structural motif was also observed for one

similar benzene-based compound[62] no connection to a fast two-dimensional growth was made. This arrangement is an alternative to the classical variant where the hydrogen bond strands are crossed instead of the molecules. In compound 3 (crystallising in $P\bar{1}$), on the other hand, each molecule forms H-bonds to two adjacent molecules, leading to a one-dimensional ribbon-like structure per definition. It is remarkable that this compound still shows a sheet-like morphology. This might be caused by the special arrangement of the molecules in the packing with respect to the crystal axes.

An important aspect with respect to the growth process of the sheets deals with the role of dipole moments for the growth mechanism. For the growth of one-dimensional rod like nanostructures – *e.g.* cyclohexane- or benzenetrisamides – it is known that dipole forces play an important role.[21] Here, every molecule possesses an intrinsic dipole moment. Within one rod, this dipole moment strongly increases and so-called macrodipoles are generated. In order to obtain an antiferroelectric crystal being energetically favoured, all macrodipoles must be compensated by an antiparallel arrangement of themselves.[63] The net dipole moment of zero is thereby achieved during the crystallisation process. This argument is also valid for the BUC5BU compound investigated in ref. 31. Even if a two-dimensional self-assembly is achieved, the intrinsic C_2 symmetry of the molecules implies an intrinsic dipole moment, too, which is only compensated due to the space group symmetry during crystallisation as well. In contrast, for the two-dimensional sheet like nanostructures presented here, dipole forces or even macrodipoles do not play a major role. The dipole moment is already cancelled in each molecule due to the inversion symmetry of the molecules themselves. So, the fast growth of the nanostructures in two directions (1 and 2) (or one direction for compound 3, respectively) giving two-dimensional nanosheets is, therefore, mainly induced by the hydrogen bond mediated donor–acceptor interactions between the appropriate molecular counterparts.

Acknowledgements

References

1 J.-M. Lehn, *Angew. Chem., Int. Ed. Engl.*, 1990, **29**, 1304.

2 S. Cantekin, T. F. A. de Greef and A. R. A. Palmans, *Chem. Soc. Rev.*, 2012, **41**, 6125.

3 Y. Yasuda, E. Iishi, H. Inada and Y. Shirota, *Chem. Lett.*, 1996, 575.

4 K. Hanabusa, C. Koto, M. Kimura, H. Shirai and A. Kakehi, *Chem. Lett.*, 1997, 429.

5 J. J. van Gorp, J. A. J. M. Vekemans and E. W. Meijer, *J. Am. Chem. Soc.*, 2002, **124**, 14759.

6 N. Shi, H. Dong, G. Yin, Z. Xu and S. Li, *Adv. Funct. Mater.*, 2007, **17**, 1837.

7 A. Bernet, R. Q. Albuquerque, M. Behr, S. T. Hoffmann and H.-W. Schmidt, *Soft Matter*, 2012, **8**, 66.

8 Y. Matsunaga, N. Miyajima, Y. Nakayasu, S. Sakai and M. Yonenaga, *Bull. Chem. Soc. Jpn.*, 1988, **61**, 207.

9 M. Gelinsky, R. Vogler and H. Vahrenkamp, *Inorg. Chem.*, 2002, **41**, 2560.

10 P. Besenius, J. L. M. Heynens, R. Straathof, M. M. L. Nieuwenhuizen, P. H. H. Bomans, E. Terreno, S. Aime, G. J. Strijkers, K. Nicolay and E. W. Meijer, *Contrast Media Mol. Imaging*, 2012, **7**, 356.

11 M. Blomenhofer, S. Ganzleben, D. Hanft, H.-W. Schmidt, M. Kristiansen, P. Smith, K. Stoll, D. Maeder and K. Hoffmann, *Macromolecules*, 2005, **38**, 3688.

12 P. M. Kristiansen, A. Gress, P. Smith, D. Hanft and H.-W. Schmidt, *Polymer*, 2006, **47**, 249.

13 F. Abraham, S. Ganzleben, D. Hanft, P. Smith and H.-W. Schmidt, *Macromol. Chem. Phys.*, 2010, **211**, 171.

14 J. Wang, Q. Dou, X. Chen and D. Li, *J. Polym. Sci., Part B: Polym. Phys.*, 2008, **46**, 1067.

15 F. Richter and H.-W. Schmidt, *Macromol. Mater. Eng.*, 2013, **298**, 190.

16 H. Nakajima, M. Takahashi and Y. Kimura, *Macromol. Mater. Eng.*, 2010, **295**, 460.

17 H. Bai, W. Zhang, H. Deng, Q. Zhang and Q. Fu, *Macromolecules*, 2011, **44**, 1233.

18 P. Song, Z. Wei, J. Liang, G. Chen and W. Zhang, *Polym. Eng. Sci.*, 2012, **52**, 1058.

19 M. Schmidt, J. J. Wittmann, R. Kress, D. Schneider, S. Steuernagel, H.-W. Schmidt and J. Senker, *Cryst. Growth Des.*, 2012, **12**, 2543.

20 M. Schmidt, J. J. Wittmann, R. Kress, H. W. Schmidt and J. Senker, *Chem. Commun.*, 2013, **49**, 267.

21 R. Q. Albuquerque, A. Timme, R. Kress, J. Senker and H.-W. Schmidt, *Chem.–Eur. J.*, 2013, **19**, 1647.

22 T. Govindaraju and M. B. Avinash, *Nanoscale*, 2012, **4**, 6102.

23 M. Stöter, D. A. Kunz, M. Schmidt, D. Hirsemann, H. Kalo, B. Putz, J. Senker and J. Breu, *Langmuir*, 2013, **29**, 1280.

24 M. B. Avinash, K. S. Subrahmanyam, Y. Sundarayya and T. Govindaraju, *Nanoscale*, 2010, **2**, 1762.

25 K. S. Novoselov, D. Jiang, F. Schedin, T. J. Booth, V. V. Khotkevich, S. V. Morozov and A. K. Geim, *Proc. Natl. Acad. Sci. U. S. A.*, 2005, **102**, 10451.

26 J. C. Meyer, A. K. Geim, M. I. Katsnelson, K. S. Novoselov, T. J. Booth and S. Roth, *Nature*, 2007, **446**, 60.

27 A. K. Geim and K. S. Novoselov, *Nat. Mater.*, 2007, **6**, 183.

28 C. N. R. Rao, A. K. Sood, K. S. Subrahmanyam and A. Govindaraj, *Angew. Chem., Int. Ed.*, 2009, **48**, 7752.

29 K. S. Subrahmanyam, P. Kumar, U. Maitra, A. Govindaraj, K. P. S. S. Hembram, U. V. Waghmare and C. N. R. Rao, *Proc. Natl. Acad. Sci. U. S. A.*, 2011, **108**, 2674.

30 J.-U. Kim, R. Davis and R. Zentel, *J. Colloid Interface Sci.*, 2011, **359**, 428.

31 R. Davis, R. Berger and R. Zentel, *Adv. Mater.*, 2007, **19**, 3878.

32 L. Seyfarth, J. Seyfarth, B. V. Lotsch, W. Schnick and J. Senker, *Phys. Chem. Chem. Phys.*, 2010, **12**, 2227.

33 E. Wirnhier, M. Döblinger, D. Gunzelmann, J. Senker, B. V. Lotsch and W. Schnick, *Chem.–Eur. J.*, 2011, **17**, 3213.

34 L. Seyfarth, J. Sehnert, N. El-Gamel, W. Milius, E. Kroke, J. Breu and J. Senker, *J. Mol. Struct.*, 2008, **889**, 217.

35 R. K. Harris, *Analyst*, 2006, **131**, 351.

36 Accelrys software inc. *MS Modeling v5.0.0.0* Copyright 2009.

37 W. A. Dollase, *J. Appl. Crystallogr.*, 1986, **19**, 267.

38 H. M. Rietveld, *J. Appl. Crystallogr.*, 1969, **2**, 65.

39 H. Toraya and F. Marumo, *Mineral. J.*, 1981, **10**, 211.

40 H. Sun, *J. Phys. Chem. B*, 1998, **102**, 7338.

41 L. W. Finger, D. E. Cox and A. P. Jephcoat, *J. Appl. Crystallogr.*, 1994, **27**, 892.

42 E. Salager, R. S. Stein, S. Steuernagel, A. Lesage, B. Elena and L. Emsley, *Chem. Phys. Lett.*, 2009, **469**, 336.

43 M. H. Levitt, *Encycl. Nucl. Magn. Reson.*, 2002, **9**, 165.

44 D. Sakellariou, A. Lesage, P. Hodgkinson and L. Emsley, *Chem. Phys. Lett.*, 2000, **319**, 253.

45 X. Zhao, W. Hoffbauer, J. S. auf der Günne and M. H. Levitt, *Solid State Nucl. Magn. Reson.*, 2004, **26**, 57.

46 J. P. Perdew and Y. Wang, *Phys. Rev. B: Condens. Matter Mater. Phys.*, 1992, **45**, 13244.

47 J. Senker, L. Seyfarth and J. Voll, *Solid State Sci.*, 2004, **6**, 1039.

48 F. W. Karau, L. Seyfarth, O. Oeckler, J. Senker, K. Landskron and W. Schnick, *Chem.–Eur. J.*, 2007, **13**, 6841.

49 D. Hirsemann, T. K.-J. Köster, J. Wack, L. van Wüllen, J. Breu and J. Senker, *Chem. Mater.*, 2011, **23**, 3152.

50 L. Seyfarth and J. Senker, *Phys. Chem. Chem. Phys.*, 2009, **11**, 3522.

51 F. Taulelle, *Solid State Sci.*, 2004, **6**, 1053.

52 J. Senker, J. Sehnert and S. Correll, *J. Am. Chem. Soc.*, 2005, **127**, 337.

53 J. Sehnert and J. Senker, *Chem.–Eur. J.*, 2007, **13**, 6339.

54 J. Sehnert, K. Bärwinkel and J. Senker, *J. Mol. Struct. (THEOCHEM)*, 2007, **824**, 58.

55 J. Sehnert, K. Baerwinkel and J. Senker, *J. Phys. Chem. B*, 2007, **111**, 10671.

56 J. Schmidt, A. Hoffmann, H. W. Spiess and D. Sebastiani, *J. Phys. Chem. B*, 2006, **110**, 23204.

57 R. Harris and A. Olivieri, *Prog. Nucl. Magn. Reson. Spectrosc.*, 1992, **24**, 435.

58 K. Eichele, *WSolids1, version 1.20.17*, Universität Tübingen, 2012.

59 Predicted NMR data calculated using Advanced Chemistry Development, Inc. (ACD/Labs) *Software V12.5* (© 1994–2013 ACD/Labs).

60 J. H. van Esch, F. Schoonbeek, M. de Loos, H. Kooijman, A. L. Spek, R. M. Kellogg and B. L. Feringa, *Chem.–Eur. J.*, 1999, **5**, 937.

61 M. de Loos, J. van Esch, R. M. Kellogg and B. L. Feringa, *Angew. Chem., Int. Ed.*, 2001, **40**, 613.

62 H.-Z. Guo, G.-D. Yin, N.-F. She and A.-X. Wu, *Acta Cryst.*, 2005, **E61**, o4062.

63 J. Senker and J. Lüdecke, *Z. Naturforsch., B: J. Chem. Sci.*, 2001, **56b**, 1089.